An experimental setup to generate narrowband bi-photons via four-wave mixing in cold atoms

N. Arias-Téllez, I. F. Ángeles-Aguillón, D. Martínez-Cara, A. Martínez-Vallejo, L. Y. Villegas-Aguilar,
L. A. Mendoza-López, Y. M. Torres, R. A. Gutiérrez-Arenas, R. Jáuregui and D. Sahagún Sánchez

*Instituto de Física, Universidad Nacional Autónoma de México, Circuito de la Investigación Científica s/n,
Ciudad Universitaria 04510 Ciudad de México, México*

I. Pérez Castillo

*Departamento de Física, Universidad Autónoma Metropolitana-Iztapalapa,
San Rafael Atlixco 186, Ciudad de México 09340, México.*

A. Ceré

Center for Quantum Technologies, 3 Science Drive 2, Singapore 117543

We present our recently-built experimental setup designed to generate near-infrared and narrow-band correlated photon pairs by inducing four-wave mixing in a cold gas of ^{87}Rb atoms confined in a magneto-optical trap. The experimental setup and its automation and control approach are described in detail. A characterization of the optical density of the atomic ensemble as well as the basic statistical measurements of the generated light are reported. The non-classical nature of the photon pairs is confirmed by observing a violation of Cauchy-Schwarz inequality by a factor of 5.6×10^5 in a Hanbury Brown – Twiss interferometer. A $1/e$ coherence time for the heralded, idler photons of 4.4 ± 0.1 ns is estimated from our observations. We are able to achieve a value of 10^4 s^{-1} pair-detection-rate, which results in a spectral brightness of 280 (MHz s)$^{-1}$. The combination of high brightness and narrow-band spectrum makes this photon-pair source a viable tool in fundamental studies of quantum states and opens the door to use them in quantum technologies.

Keywords: Bi-photons; quantum networks; four wave mixing; cold atoms; quantum information.

1. Introduction

Since the 1970s sources of entangled photon pairs are an important pillar in quantum optics. On the one hand they enable to probe the foundations of quantum mechanics and, on the other, they are a cornerstone in the development of novel quantum technologies. Time-correlated photon pairs were firstly generated by inducing spontaneous parametric down conversion (SPDC) in non-linear crystals [1]. This was subsequently followed by observing quantum entanglement for the first time in photons emitted by atomic gases subjected to a four-wave mixing (FWM) process [2]. In addition to serving a broad span of basic research during several decades, experimental methods based on these two non-linear processes play an important role in the *second quantum revolution*, the on-going development of technologies that is set to change – even – daily life paradigms [3].

With SPDC, researchers have invented techniques yielding an outstanding feedback between science and technology. Several of those methods are now the platform for both exploring the laws of quantum physics and for developing applications of quantum optics such as cryptography and metrology [4]. The role of FWM as a main character in quantum optics and its applications is spread in history. After subsequent experiments establishing methods for testing the Bell inequalities [5], this non-linear process attracted

back major attention after the proposal by Duan, Lukin, Cirac and Zoller for building a quantum repeater based on atomic gases [6]. Such repeater has not yet been achieved, however, the challenging quest for it has engaged researchers in the development of long-lived and efficient quantum memories [7, 8], and the generation of photon pairs that can – in principle – be tailored by means of the exquisite control over the atomic states provided by precision spectroscopy.

Motivated by the creation of hybrid quantum systems [9, 10], time-correlated photon pairs were generated from cold atoms in a seminal work by Kuzmich *et al.* [11]. Their potential as a narrowband source of photon pairs suitable for interacting with atoms and thus, for creating quantum systems, was thereafter demonstrated [12]. In this context, it is desirable to generate photons that can excite specific dipole lines connecting predetermined atomic states, and to generate photons in the telecommunications regime. In this way, one would be able to imprint information into a quantum memory and simultaneously send it far away through optical fibers. In principle, this can be achieved with several *diamond* schemes of transitions within the rich electronic structure of the alkali elements [13] (see Fig. 1).

Photons generated by FWM in laser-cooled atoms have naturally a bandwidth comparable to the decay rate of their states (in the order of a few MHz). Using electromagnetically induced transparency it is possible to achieve bandwidths be-
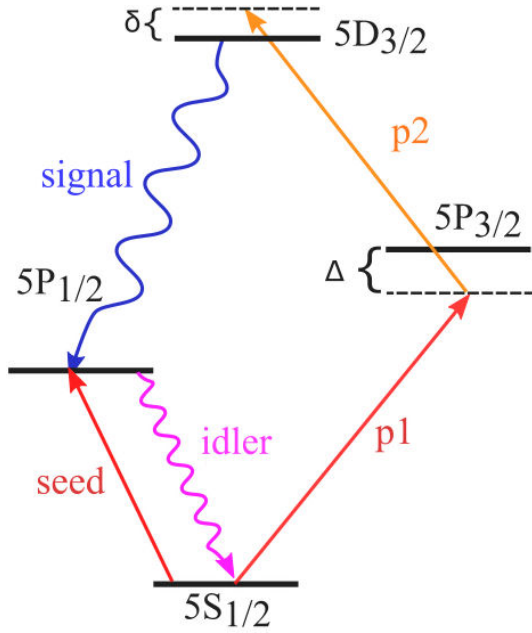
FIGURE 1. Simplified schematics of the FWM diamond configuration implemented in our experiments. It involves a ladder transition followed by a cascade decay in the ^{87}Rb electronic structure: $p1$ represents a laser beam stabilized to its $5S_{1/2} \rightarrow 5P_{3/2}$ and $p2$ depicts an optical field resonant to the $5P_{3/2} \rightarrow 5D_{3/2}$ transition. Both detunings Δ and δ are important parameters for the non-linear process. The signal photons are emitted when atoms decay from the $5D_{3/2}$ to the $5P_{1/2}$ state; idler photons are parametric decay happening generated by the $5P_{1/2} \rightarrow 5S_{1/2}$ decay. A seed laser, tuned to the $5S_{1/2} \rightarrow 5P_{1/2}$ transition, is used for amplifying the FWM signal in the pre-alignment procedure. However, it is switched off during experiments as explained in Sec. 4.

low one MHz [14]. A bandwidth of 20 MHz has been reached by inducing FWM on the diamond scheme without optically filtering the generated light [15]. It can be further narrowed below 8 MHz by introducing a resonant cavity [16]. In setups of this kind, it is possible to generate photonic Bell states; entanglement of linear momentum [17, 18] and orbital angular momentum [19] has also been observed between the signal and idler counterparts. These states are directly related to the atomic degrees of freedom and the dynamics induced by the FWM process. Therefore, they are controllable with the characteristics of the laser beams pumping the non-linear process.

Within this context, we present our experimental setup for generating photon pairs from cold atoms as well as measurements of the coherence of the photons to show that it is, indeed, a narrowband and bright source of non-classical light. The remainder of this article is organized as follows. In Sec. 2 we describe a theoretical framework of FWM in atoms, from which the phase matching conditions are derived. This is followed by a model of the cascade decay useful in the description of the generated bi-photon state (Sec. 3). Next, in Sec. 4, we describe in detail the experimental setup. There, we emphasize basic concepts of the applied methods, and describe technical aspects particular to our machine and its essential experimental protocols. In Sec. 5 we show the experimental

results and their analysis. From their second-order crossed-correlation function we estimate the coherence time of the idler as heralded by the signal photons. With this time we compute the spectral brightness of our source for typical experimental conditions. Following that, we verify the chaotic time statistics of the signal and idler photons in terms of the corresponding auto-correlation measurements. We then use both results to evaluate the Cauchy-Schwartz inequality, showing a strong violation. Finally, in Sec. 6, we conclude the reported work and give an outlook toward our research interests.

2. Four-wave mixing in atoms

Four-wave mixing is possible in center-symmetric media, such as an atomic gas. Figure 2 illustrates its implementation in a cold atomic gas within a magneto-optical trap (MOT). The pump beams $p1$ and $p2$ target the cloud of cold atoms. Their field overlap in the same volume where the signal (s) and idler (i) photons are generated and eventually detected with avalanche photodiodes.

The stimulated atomic transitions come along with isotropic spontaneous parametric emission of photons. However, a proper phase relationship between the interacting waves guarantees constructive addition of the amplitude contributions from different locations and emission times inside the atomic gas. Both processes can be described in terms of the electric susceptibilities: isotropic spontaneous emission in terms of first order susceptibility $\chi^{(1)}$ and FWM in terms of the third order susceptibility $\chi^{(3)}$. The later relates the polarization of atoms with the involved electric fields as

$$\mathbf{P}_j^{(+)}(\omega_{s,i}) = \epsilon_0 \sum_{klm} \chi_{jklm}^{(3)} \left(\mathbf{E}_{p1}^{(+)}\right)_k \left(\mathbf{E}_{p2}^{(+)}\right)_l \left(\hat{\mathbf{E}}_{i,s}^{(-)}\right)_m , \quad (1)$$

inside the material. In this case the polarization acts as a source of quantum light at the signal or idler angular frequencies (ω_s or ω_i). In Eq. (1), ϵ_0 is the electric permittivity of vacuum. The two pump electric fields $\mathbf{E}_{p1}$ and $\mathbf{E}_{p2}$ are written in terms of plane wave modes
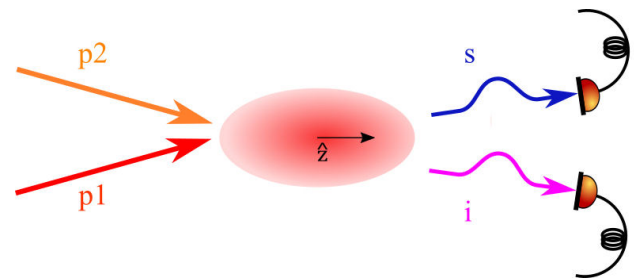

FIGURE 2. Generic schematics of FWM in cold atomic gases. Two pump beams, $p1$ and $p2$, are overlapped in the center of a MOT. A signal (s) and idler (i) photon pair is generated inside the interaction volume.

$$\mathbf{E}_p = \frac{1}{2}\left(\mathbf{E}_p^{(+)} + \mathbf{E}_p^{(-)}\right),$$

$$\mathbf{E}_p^{(+)}(\mathbf{r}, t) = \mathbf{E}_p e^{i(\mathbf{k}_p \cdot \mathbf{r} - \omega_p t)}, \quad (2)$$

$$\mathbf{E}_p^{(-)}(\mathbf{r}, t) = \mathbf{E}_p^* e^{-i(\mathbf{k}_p \cdot \mathbf{r} - \omega_p t)},$$

with $p = p1, p2$; the angular frequencies ω_{p1} and ω_{p2}, and the wave vectors $\mathbf{k}_{p1}$ and $\mathbf{k}_{p2}$. The pump electric fields are well represented by classical fields because they are laser beams. However, the signal an idler fields must be described using the quantum theory,

$$\hat{\mathbf{E}}_{s,i}^{(+)}(\mathbf{r}, t) = \frac{1}{2\pi} \int d\omega_{s,i} d\mathbf{k} \sqrt{\frac{2\hbar\omega_{s,i}}{c\epsilon_0 A}} \hat{a}_{s,i}(\omega_{s,i}, \mathbf{k}_{s,i}, \boldsymbol{\epsilon}_{s,i})$$
$$\times \boldsymbol{\epsilon}_{s,i}(\mathbf{k}_{s,i}) e^{i(\mathbf{k}_{s,i} \cdot \mathbf{r} - \omega_{s,i} t)} \delta(\omega_{s,i} - |\mathbf{k}_{s,i}|), \quad (3)$$

where ϵ denotes the polarization vector and A an effective cross-section area introduced for quantization purposes. The creation and annihilation operators, $\hat{a}_{s,i}^\dagger$ and $\hat{a}_{s,i}$, satisfy the standard commutation relations for all the variables determining the mode,

$$\left[\hat{a}_{s,i}(\omega, \mathbf{k}, \boldsymbol{\epsilon}), \hat{a}_{s,i}^\dagger(\omega', \mathbf{k}', \boldsymbol{\epsilon}')\right] = \delta_{\epsilon,\epsilon'}\delta(\omega - \omega')\delta(\mathbf{k} - \mathbf{k}');$$

$\hat{\mathbf{E}}_{s,i}^{(-)}$ is the Hermitian conjugate of the operator $\hat{\mathbf{E}}_{s,i}^{(+)}$.

In the interaction picture, the relevant effective Hamiltonian of the atomic system, whose properties are encoded in the susceptibility $\chi^{(3)}$ and the four electric fields, is [20]

$$\hat{\mathbf{H}}_I = \frac{\varepsilon_0}{4} \sum_{jklm} \int_V d\mathbf{r} \chi_{jklm}^{(3)}$$
$$\times \left(\mathbf{E}_{p1}^{(+)}\right)_k \left(\mathbf{E}_{p2}^{(+)}\right)_l \left(\hat{\mathbf{E}}_s^{(-)}\right)_m \left(\hat{\mathbf{E}}_i^{(-)}\right)_j + \text{H. c.}, \quad (4)$$

here $d\mathbf{r}$ denotes the differential of the volume V where the four fields overlap. Considering $p1$ and $p2$ as co-propagating plane waves simplifies the mathematical visualization of the physical process and, even more important, resembles the system created in our setup. By integrating the Hamiltonian (4) over the complete space, one finds two phase-matching conditions, that can be interpreted as conservation rules,

$$\mathbf{k}_{p1} + \mathbf{k}_{p2} = \mathbf{k}_s + \mathbf{k}_i, \quad (5)$$

for linear momentum and

$$\omega_{p1} + \omega_{p2} = \omega_s + \omega_i, \quad (6)$$

for energy. Equation (5) relates the direction of the generated photons with that of the pump beams. In this case all are co-linear.

3. Coherence of the generated quantum states

The time statistics of the photon pairs can be evaluated with the second-order correlation function

$$G^{(2)}(\mathbf{r}_1, t_1; \mathbf{r}_2, t_2) = ||\hat{\mathbf{E}}_s^{(+)}(\mathbf{r}_1, t_1)\hat{\mathbf{E}}_i^{(+)}(\mathbf{r}_2, t_2)|\psi\rangle||^2, \quad (7)$$

which describes the probability of a pair of photodetection events with $\mathbf{r}_{1,2}$ being the positions where each photon is detected, and t_1 and t_2 being the detection times.

The second-order correlation function may be built from the spontaneous decay of a single atom from a second excited state [21]. Although this model does not account effects yielded by the ensemble, it has turned out useful for investigating the generated time-frequency entanglement within the cascade emission scheme [31] and it is useful to make a basic coherence analysis of the generated quantum states, see Section 5..

For a cascade decay of a single atom, resulting in a two-photon state $|\psi\rangle$, this function can be written as [21]

$$G^{(2)}(\mathbf{r}_1, t_1; \mathbf{r}_2, t_2) = \Psi^{(2)}(\mathbf{r}_1, t_1; \mathbf{r}_2, t_2)$$
$$\times \Psi^{(2)\star}(\mathbf{r}_1, t_1; \mathbf{r}_2, t_2), \quad (8)$$

where

$$\Psi^{(2)}(\mathbf{r}_1, t_1; \mathbf{r}_2, t_2) = \langle 0|\hat{\mathbf{E}}_s^{(+)}(\mathbf{r}_1, t_1)\hat{\mathbf{E}}_i^{(+)}(\mathbf{r}_2, t_2)|\psi\rangle, \quad (9)$$

is the transition amplitude from the two-photon state $|\psi\rangle$ to the vacuum state $|0\rangle$, the only one remaining after the introduction of an identity-operator resolution preceding the operator $\hat{E}_s^{(+)}(\mathbf{r}_1, t_1)$ in terms of photonic number states [Eq. (7)].

In the next paragraphs an expression of $|\psi\rangle$ corresponding to the asymptotic two-photon steady state is derived.

3.1. Heralding effect

For quantum information applications, it is important to know when a single photon is likely to be detected. Photons emitted in cascade facilitate this due to the intrinsic delay between photons of each pair. This can be evaluated from their second order correlation function which can be calculated by solving the evolution equation of the atom, idler and signal electromagnetic field state,

$$\frac{d}{dt}|\psi(t)\rangle = -\frac{i}{\hbar}\tilde{H}_I|\psi(t)\rangle. \quad (10)$$

Instead of solving the Maxwell-Bloch equations, we assume a simplified scheme where just the atomic states participating in the cascade transitions are involved [21]. This scheme considers a single atom, it does not describe the pumping procedure, and incorporates the electromagnetic environment effects on the atomic states through the decaying rates. The relevant atom- electromagnetic field state is expressed as

$$|\psi(t)\rangle = c_\alpha(t)|\alpha, 0_k, 0_q\rangle + \sum_k c_{\beta k}(t)|\beta, 1_k, 0_q\rangle$$
$$+ \sum_{k,q} c_{\gamma kq}(t)|\gamma, 1_k, 1_q\rangle. \quad (11)$$

For the FWM configuration in Fig. 1, the first term of this equation corresponds to the atomic second-excited state $|\alpha\rangle = 5D_{3/2}$ with zero signal or idler photons, the second term is linked to the atomic first excited state $|\beta\rangle = 5P_{1/2}$ with one signal photon occupying one vacuum mode k and zero idler photons, and the last term stands for the ground state $|\gamma\rangle = 5S_{1/2}$ with the presence of one signal and one idler photon in the mode q. The effective Hamiltonian in the interaction picture under the rotating-wave approximation is

$$\tilde{H}_I = \hbar \sum_k \left(g_{\alpha\beta}^{sk} \sigma_+^{(1)} \hat{a}_{ik} e^{i(\omega_{\alpha\beta}-\omega_k)t} + H.c \right)$$
$$+ \hbar \sum_q \left(g_{\beta\gamma}^{iq} \sigma_+^{(2)} \hat{a}_{sq} e^{i(\omega_{\beta\gamma}-\omega_q)t} + H.c \right), \qquad (12)$$

where ω_{if} is the frequency corresponding to the energy separation between states for each $|i\rangle \rightarrow |j\rangle$ decay and, the raising operators are $\sigma_+^{(1)} = |\alpha\rangle\langle\beta|$ and $\sigma_+^{(2)} = |\beta\rangle\langle\gamma|$. In Equation (12) the coupling constants,

$$g_{ij}^{lk} = \sqrt{\frac{\hbar\omega_k}{2\epsilon_0 V}} \mathbf{d}_{ij} \cdot \boldsymbol{\epsilon}_k(\mathbf{k}) e^{i\mathbf{k}\cdot\mathbf{r}}, \qquad (13)$$

are the analogous to Rabi frequencies for single photons; they are defined in terms of the dipole transition matrix element $\mathbf{d}_{ij}$.

One can solve for the coefficients $c(t)$ of the state $|\psi(t)\rangle$ by inserting Eqs. (11-12) into Eq. (10). Introducing the Γ_α and Γ_β the decay rates of the states $|\alpha\rangle$ and $|\beta\rangle$, the system of differential equations

$$\dot{c}_\alpha(t) = -\frac{\Gamma_\alpha}{2} c_\alpha(t),$$
$$\dot{c}_{\beta k}(t) = -i g_{\alpha\beta}^{sk} e^{i(\omega_{\alpha\beta}-\omega_k)t} c_a(t) - \frac{\Gamma_\beta}{2} c_{\beta k}(t), \qquad (14)$$
$$\dot{c}_{\gamma kq}(t) = -i g_{\beta\gamma}^{iq} e^{i(\omega_{\beta\gamma}-\omega_q)t} c_{\beta k}(t),$$

is obtained. The decay rate $\Gamma_\beta = 1/(2\pi\tau_c)$ determines a coherence time for the heralded idler photons. The coefficients $c(t)$ are constrained to the initial conditions $c_\alpha(0) = 1$ and $c_{\beta k}(0) = c_{\gamma kq}(0) = 0$ in order to resemble a cascade decay.

From the first equation

$$c_\alpha(t) = \exp\left(-\Gamma_\alpha t/2\right)$$

is obtained trivially. The second coefficient

$$c_{\beta k}(t) = i g_{\alpha\beta}^{sk} \frac{e^{[i(\omega_k-\omega_{\alpha\beta})-\Gamma_\alpha/2]t} - e^{-\Gamma_\beta t/2}}{i(\omega_k - \omega_{\alpha\beta}) - (\Gamma_\alpha - \Gamma_\beta)}, \qquad (15)$$

is readily derived by inserting this solution into the corresponding equation and integrating; plugging this solution of $c_{\beta k}(t)$ into the third differential equation yields a state $|\psi(t)\rangle$ which allows an approximate description of a transient regime studied in Ref. [22]. There, fast decay times and oscillations that depend on the detunings and intensities of the pump fields occur. Here, we are interested in a steady state that results from the long time limit

$$c_{\gamma kq}(\infty) = \frac{g_{\alpha\beta}^{sk}}{i(\omega_k + \omega_q - \omega_{\alpha\beta} - \omega_{\beta\gamma}) - \Gamma_\alpha/2}$$
$$\times \frac{g_{\beta\gamma}^{iq}}{i(\omega_q - \omega_{\beta\gamma}) - \Gamma_\beta/2}; \qquad (16)$$

the other two coefficients vanish, $c_\alpha(\infty) = c_{\beta k}(\infty) = 0$. Note that $c_{\gamma kq}(\infty)$ determines the conditional probability of finding the atom at the lowest level and the two photons derived from a previous decay. Thus, its squared value does not represent an atomic population. As expected, these equations yield Lorentzian profiles for the two cascade decays.

The probability amplitude given by Eq. (9) can now be evaluated for the asymptotic steady state

$$|\psi(\infty)\rangle = \sum_{kq} c_{\gamma kq}(\infty)|\gamma, 1_k, 1_q\rangle. \qquad (17)$$

Assuming a continuous vacuum spectrum, the correlation amplitude $\Psi_{si}^{(2)}$ can be written as an integral over the wave vectors $\mathbf{k}$ and $\mathbf{q}$. After solving its angular part in spherical coordinates one arrives to

$$\Psi_{si}^{(2)}(\mathbf{r}_1, t_1; \mathbf{r}_2, t_2) = \Psi_0 \int\limits_0^\infty \int\limits_0^\infty dk dq \frac{e^{-ickt_1}(e^{-ik\Delta r_1} - e^{ik\Delta r_1})}{[i(ck + cq - \omega_{\alpha\gamma}) - \Gamma_\alpha/2)]} \frac{e^{-icqt_2}(e^{-iq\Delta r_2} - e^{iq\Delta r_2})}{[i(cq - \omega_{\beta\gamma}) - \Gamma_\beta/2)]}, \qquad (18)$$

with Ψ_0 defined as

$$\Psi_0 = \frac{(2\pi)^2 k_0 q_0 g_{\alpha k} g_{\beta q}}{\Delta r_1 \Delta r_2}, \qquad (19)$$

where $k_0 = (\omega_{\alpha\gamma} - i\Gamma_\alpha/2)/c - q_0$ and $q_0 = (\Gamma_\beta/2 + \omega_{\beta\gamma})/c$; $\Delta r_{1,2}$ correspond to the distances between the position of the atom, where each photon was emitted, and the position where each photon is detected. The integrand of Eq. (18) corresponds to probabilities given by the product of two

Lorentzians; looking at the integrand structure it is observed that the extension of the lower limit of the integrals over the k and q to $-\infty$ is a reliable approximation. Then, the residue theorem of Cauchy leads to

$$\Psi_{si}^{(2)}(t_1, t_2) = 2\pi^2 \Psi_0 e^{-(i\omega_{\alpha\beta}+\Gamma_\alpha/2)t_s} \Theta[t_s]$$
$$\times e^{-(i\omega_{\beta\gamma}+\Gamma_\beta/2)(t_i - t_s)} \Theta[t_i - t_s], \qquad (20)$$

where

$$t_s = t_1 - \Delta r_1/c,$$

and

$$t_i = t_2 - \Delta r_2/c.$$

In Eq. (20), t_s and t_i incorporate directly the retardation effects for the signal and idler photons. Finally, the second-order correlation function can be written as

$$G_{si}^{(2)}(t_s, \Delta t) = G_{t_s} e^{-\Gamma_\beta \Delta t} \Theta(\Delta t), \qquad (21)$$

with amplitude

$$G_{t_s} = |2\pi^2 \Psi_0|^2 e^{\Gamma_\alpha t_s}$$

and $\Delta t = t_i - t_s$. This equation shows that t_s is a trigger time for a sudden rise of the probability of detecting an idler photon to its maximum value followed by an exponential decay with a rate Γ_β. The same result can be found with a treatment based on Green functions [23]. In our case, $\Gamma_\beta = 36$ MHz and $\Gamma_\alpha = 0.6$ MHz.

This treatment involves a single atom, it does not account for collective effects. However, corrections to this scheme can be estimated from effective decay rates [24] as described in Sec. 4.2.1.

4. Experimental setup

Two laser frequencies are required for cooling atoms and another three different frequencies are employed to induce FWM in the atoms. All of them are stabilized by common saturation absorption spectroscopy techniques. The core of this setup is a standard MOT of ^{87}Rb atoms. It is created inside an almost portable vacuum system.[i] This MOT confines typically over 10^7 atoms with an optical density (OD) that can be chosen to take any value between 5 and 22. The control and data acquisition systems are a combination of commercial equipment with home built electronics, controlled by our purpose-developed software. Experiments are performed in a duty cycle that has an atom loading period followed by FWM pulse, when the MOT is briefly released. The photon collection optics has been arranged with two Hanbury-Brown-Twiss interferometers and with two setups for measuring polarization correlations between the signal and idler photons.

4.1. Laser system

As shown in Fig. 3, the laser system is built in a modular fashion. Each gray box represents an optical arrangement that
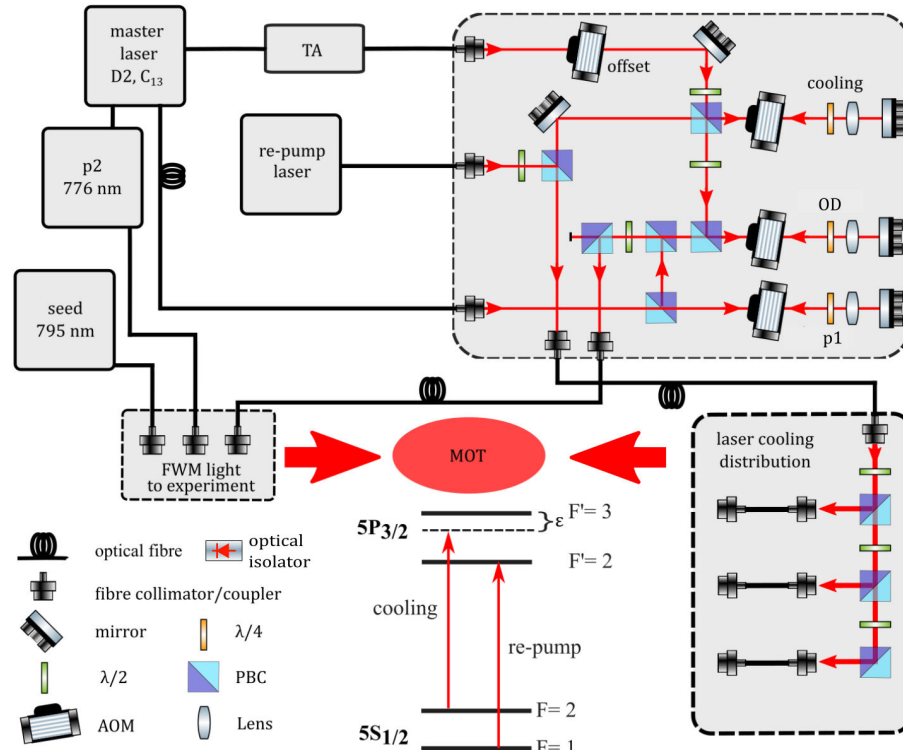

FIGURE 3. Block diagram of our experiment. The master laser is located at the left, top corner. It delivers frequency-stabilized light to seed our tapered amplifier (TA) for laser cooling, a small portion of its light is further tuned to prepare the $p1$ beam and the third output provides the first photon in the two step spectroscopy setup for the $p2$ laser that is described in Sec. 4.1.1. In addition to the spectroscopy arrangements (gray boxes with solid borders), the light is fine tuned and prepared in polarization on the distribution boards (gray boxes with dashed borders).

has been setup on a breadboard made of granite with the optical posts attached to it with instant glue. As reported in Ref. [25], we found this to be a convenient solution because it allows building compact optical setups that remain stable for years.[ii] The boxes with solid borders represent setups of spectroscopy; boxes with dashed borders are optical arrangements that distribute light. The five frequencies required for inducing FWM in the MOT are generated by three commercial lasers (Moglabs: LDL and CEL002) and one home-built extended cavity diode laser (ECDL).

The master laser is located at the left, top corner of Fig. 3. It emits light locked to the crossover between the $5S_{1/2}$, F = $2 \rightarrow 5P_{3/2}$, F' = 3 and the $5S_{1/2}$, F = $2 \rightarrow 5P_{3/2}$, F' = 2 transitions to three different points around the setup. About one third of it (20 mW) seeds a tapered amplifier (TA) that generates up to 2 Watts of light that are further tuned with AOMs for laser cooling and for measuring the optical density OD. On the AOM board, the amplified light is offset by + 60 MHz with a single-pass OAM. This leaves it -151.6 MHz from the cooling transition. Thus we can optimize the laser cooling through its detuning ε, and implement the OD measurements described in Sec. 4.2.1 with an appropriate control of the detuning Δ of its probe beam with an AOM double passes of + 76 MHz in each case. To close the two-level system required for laser cooling the re-pump beam is combined with the cooling light at the polarizing beam splitter right before its output port as depicted in Fig. 3. The re-pump laser is home-made, its design was inspired on the Littrow version reported on [25].[iii] Clockwise, around the master laser in Fig. 3, its second output supplies $p1$ light to the AOM board. In order to avoid incoherent scattering from the first step of the FWM it is convenient to set a large detuning Δ (Fig. 1). Its optimal value was found around -60 MHz in our experiments. This is achieved by bypassing the offset AOM with the $p1$ beam, which is delivered to the FWM board after double passing its AOM. To complete the FWM frequencies we have the seed and the $p2$ lasers. The former is stabilized to the $5S_{1/2}$, F = $2 \rightarrow 5P_{1/2}$, F' = 2 transition with standard saturated absorption spectroscopy. As described in Sec. 4.4, it is used for alignment purposes without further frequency tuning.

4.1.1. Two-photon spectroscopy

The $p2$ laser, depicted in Fig. 3, is a source of light at 776 nm intended to stimulate the $5P_{3/2} \rightarrow 5D_{3/2}$ transition in the MOT. This is the second step of a double atomic transition thus, it has a relatively low probability to happen. A laser stabilization scheme, based on fluorescence lock-in detection, is suggested in Ref. [26]. However, the saturated absorption method used in [27] to probe the $5D_{5/2}$ state in room-temperature atoms works well also for the $5D_{3/2}$ state if their partial pressure is increased by heating up the spectroscopy cell. Implementing polarization spectroscopy [28] yields similar results. However, temperature drifts due to the cell heating makes stabilization hard to establish in the long term.
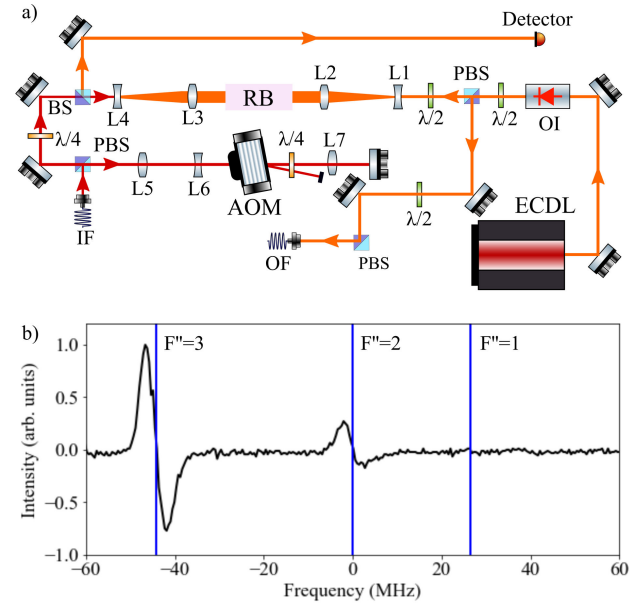

FIGURE 4. Schematics of the two-photon spectroscopy setup a) and error signal obtained with it b). The red beam depicts light at 780 nm for exciting the first step of the ladder; the orange beam represents the second photon, at 776 nm. IF indicates the input fiber of the 780 nm beam and OF indicates the output fiber of $p2$ going to the experiment. Optical elements are labeled following the same code as in Fig. 3.

Figure 4a) shows a schematics of our two-photon spectroscopy setup. About 3 mW of the master laser light is delivered to it through the optical fiber IF. The frequency of this beam is shifted by 2×70 MHz. This compensates the -60 MHz detuning on the $p1$ beam from resonance and enables a convenient scanning of δ with the $p2$ laser. The same AOM modulates the frequency of the master laser by 250 kHz as required for saturated absorption spectroscopy. This beam is then sent through the cell as the pump with horizontal polarization.

The p2 light is generated by a cateye ECDL [29] (MOGLABS, CEL002). Its frequency is scanned across all the hyperfine levels of the $5D_{3/2}$ state. Approximately 3 mW from this laser enters the spectroscopy cell as the probe beam with linear polarization. Both beams counter-propagate and fully overlap to cancel Doppler broadening and to increase the interaction volume. The later is further incremented by expanding their $1/e^2$ width from 1 to 4 mm, see Fig. 4a).

Modulating the frequency of the pump beam also modulates its interaction with atoms inside the spectroscopy cell. This facilitates to derive the saturation signal assisted with a servo-loop circuit and a low-pass filter [30], yielding a 20 mV peak-to-peak error signal in this case. This is a factor of 15 smaller than typical traces probing D lines with saturation absorption spectroscopy. Heating the spectroscopy cell enhances the obtained signal, making it suitable for locking a laser with standard electronics. Two power resistors of 10 Ω carrying 2 A are attached to the base of the cell. Thus, a stable temperature close to 70°C is reached after one hour of

heating. Figure 4b) shows a typical error trace that serves for locking the $p2$ laser. The blue lines cross the curve at the three points in which we can lock it. For the experiments reported here we used the $F' = 3$ to $F'' = 3$ of the $5P_{3/2}, F' \rightarrow 5D_{3/2}, F''$ transition. If one desires locking the laser to $F'' = 1$ or 2, it would be necessary to further increase the temperature of the cell. This laser produces 25 mW of stabilized light. Its detuning δ (Fig. 1) is controlled with the AOM in the range - 12 to + 12 MHz with respect to the $5P_{3/2}, F' = 3 \rightarrow 5D_{3/2}, F'' = 3$ transition.

4.2. Vacuum system and MOT

As depicted in Fig. 5, the vacuum system has six elements only. Its simplicity grants full optical access and enables to reach ultra-high vacuum (UHV). The science cell (1) is an octagon made of quartz with windows anti-reflection coated for 780 nm light. The top and bottom windows have a 1.375 in diameter whereas the diameter of the lateral windows is 1 in. This cell is connected to a CF30 cube that holds all the vacuum system (2). Its vertical branch runs upwards towards a hybrid ion-sublimation pump [NEXTorr D 100-5, (3)]. Lastly, (4) is a tee connecting a four-conductor feedthrough (5) and a UHV valve (6). The feedthrough connects independently two Rubidium dispensers and the valve is used for plugging the system to a pumping station for building vacuum from atmospheric pressure. With this system it is possible to reach pressures below 10^{-10} Torr without baking. Ultra-high vacuum is not a necessary requirement for creating a MOT. However, in it one can transfer atoms to a dipole or a magnetic trap. With those traps it is possible to change
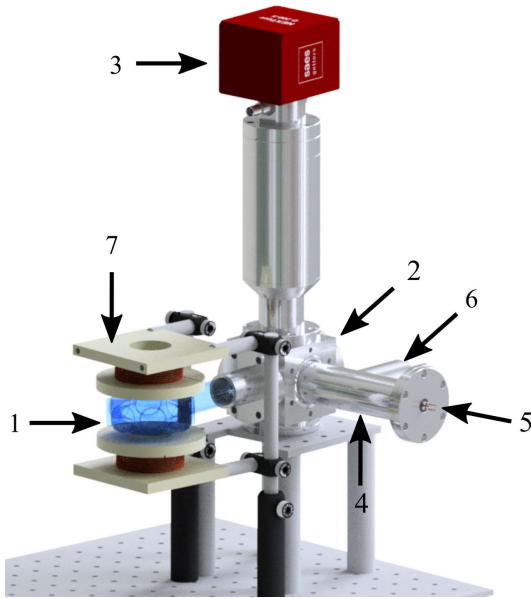

FIGURE 5. Render of our vacuum system. The components are: (1) science cell, (2) CF30 cube, (3) vacuum pump (NEXTorr D 100-5), (4) tee, (5) feedthrough for Rubidium dispensers, (6) UHV valve and (7) MOT coils.

the shape of the atom cloud. This would open the possibility of modulating the superradiance generated by collective effects throughout the FWM process [31].

Figure 5 also shows the MOT coils (7). They have 13 layers, with 9 windings each, of 13 AWG wire. The coil formers were 3D printed and designed to preserve full optical access to the science cell. Once arranged in an anti-Helmholtz configuration this coils generate a magnetic quadrupole field with axial gradients up to 30 Gcm^{-1}, driving 8 A, with a stable temperature under 60°C. We found easier to align the MOT and FWM beams for experiments without compensation coils. The three MOT beams (not shown) are delivered from their distribution board, depicted in Fig. 3. They form a 3D retro-reflection laser cooling arrangement. Each beam is about 20 mm in diameter and carries 13 mW of light that is -24 MHz detuned from the cooling transition. As explained below, less than 10 mW of evenly distributed re-pump light are enough to saturate the number of trapped atoms.

4.2.1. Optical density

Collective quantum-optical phenomena depend upon the amount of emitting atoms. For the light generated via FWM this is determined by the number of atoms simultaneously interacting with both pump beams. A direct way to find out this number is by measuring OD in the atomic cloud. Together with its shape, this parameter governs the influence that superradiance may have on the relaxation of atoms from their excited states and, consequently, on the bi-photons coherence properties [31].

The absorption of a near-resonance laser beam traveling through an atomic sample is described by the Beer's Law,

$$\frac{dI}{dz} = -\hbar\omega\gamma_p n, \tag{22}$$

where I is its intensity, z is the propagation distance through the atomic sample, n is the density of atoms, ω is the angular frequency of the transition being probed and γ_p is the total scattering rate given by [32]

$$\gamma_p = \frac{s_0\Gamma/2}{1 + s_0 + (2\Delta/\Gamma)^2}. \tag{23}$$

In Eq. (23), Γ is the excited state natural decay rate; $\Delta = \omega_l - \omega$ is the laser detuning from resonance; $s_0 = I/I_{sat}$ and I_{sat} are the on-resonance saturation parameter and intensity, respectively. For a low saturation parameter ($I \ll I_{sat}$) Eq. (23) simplifies to

$$\gamma_p = \frac{I\Gamma}{2I_{sat}} \frac{\Gamma^2}{\Gamma^2 + 4\Delta^2}. \tag{24}$$

Substituting Eq. (24) into Eq. (22) and integrating along z gives rise to the ratio of intensity absorption

$$\frac{I}{I_0} = \exp\left(-OD\frac{\Gamma^2}{\Gamma^2 + 4\Delta^2}\right), \tag{25}$$

where I_0 is the intensity of the probe beam before been scattered by atoms. The optical density OD is defined in terms
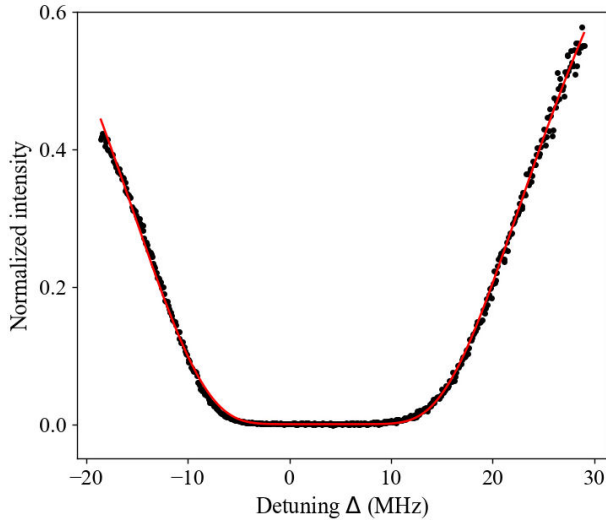
FIGURE 6. Normalized intensity I/I_0 as a function of the probe beam detuning. In black is the experimental data and the red curve is a fit using Eq. (25).
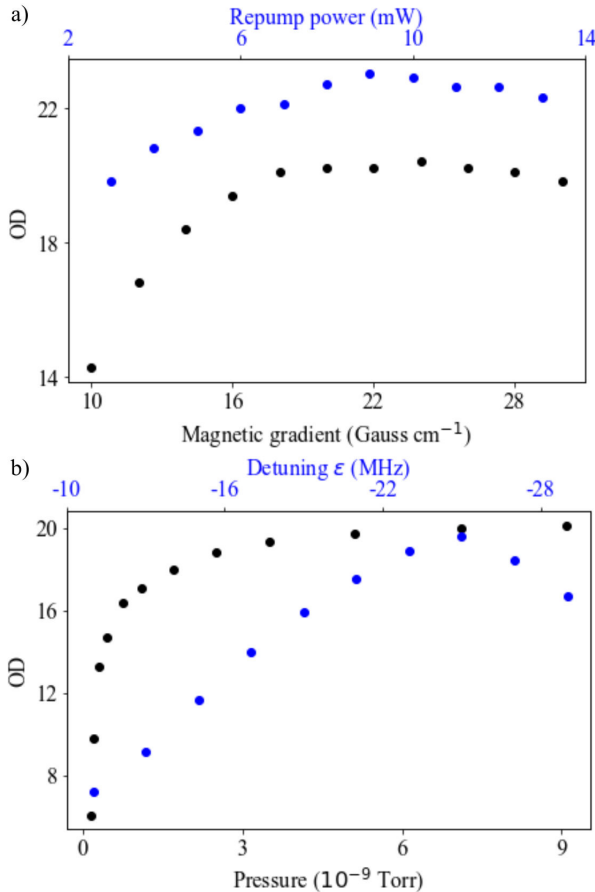

FIGURE 7. Dependency of OD on a) the power of the re-pump beam (blue) and on the field gradient produced by the coils (black) and; b) on the detuning ε (blue) and on the partial pressure of Rubidium inside the vacuum chamber (black).

of the on-resonance cross section σ_0, the atom number N, and the light mode transverse area A as $OD = N\sigma_0/A$.

To measure OD we target the center of the atomic cloud with a low intensity probe beam, scan its frequency from -18 MHz to $+25$ MHz around the cooling transition and monitor its absorption with a photodiode. We acquire three series of data: (i) with the MOT and probe beam on, (ii) without the MOT and the probe on, and (iii) with the MOT on and probe switched off. Figure 6 displays a typical absorption data set (black dots) and curve (red) fitted to it with Eq. (25). There, Γ is set to 6.065 MHz [33] and OD is left as the only free parameter. The experimental points displayed on Fig. 6 were obtained with a $I_0 = 0.5$ mW cm^{-2}, horizontally polarized probe beam. The asymmetry around resonance is originated by the Zeeman sub-levels that are involved in the probed transition. From the fit we can estimate the atom number. For this experiments the probe beam is around 0.008 cm^2 and $\sigma_0 = 2.907 \times 10^{-9}$ cm^2 for vertically polarized light. Thus, in this case $OD = 20 \pm 0.2$, which is equivalent to 5×10^7 absorbing atoms.

The optical density of a MOT mostly depends on: (i) the detuning ε of its cooling light and its power, (ii) partial pressure of Rubidium inside the vacuum chamber, (iii) the power of the re-pump beam and, (iv) the gradient of magnetic field given by its coils. Figure 7a) displays the OD of our MOT as a function of the gradient (black dots). To get these data the other parameters were fixed to values established during a previous optimization: $\varepsilon = $ - 23 MHz, a pressure of 10^{-9} torr and (iii) 8 mW of re-pump power evenly distributed among the MOT beams. The blue dots in Fig. 7a) were taken to characterize OD as a function of the re-pump power. All parameters were kept at the mentioned values except the magnetic gradient which was left saturated at 22 Gauss cm^{-1}. In this case OD increases approximately linearly up to about 8 mW, which was the power left on for the next data set.

The blue dots in Fig. 7b) illustrate OD as a function of ε. Note that, as well as with the re-pump power, this dependency is approximately linear down to about - 23 MHz. Finally, the black dots in Fig. 7b) were taken with this detuning. They show the OD behaviour as a function of the partial pressure of Rubidium inside the vacuum chamber. The first experimental data depicts a measurement of $OD = 6$ for a partial pressure of Rubidium below 0.1×10^{-11} torr; these experiments were taken with a 1.5×10^{-11} torr base pressure. Every reading above this value is a direct measure of the Rubidium atoms available to be trapped, which is controlled by the current driven through the dispenser. The experimental data display a clear non-linear behaviour that saturates until the MOT cannot longer increase the number of confined atoms.

From the data shown in Fig. 7 one can conclude that OD can be varied from 9 to 22 in our setup given that the MOT is fully loaded. Most of this range is conveniently covered by the detuning ε as the knob. The rest of it may be completed by using the dependency of OD on the re-pump power. All measurements depicted in Fig. 7 were carried out with a total laser cooling power of 60 mW evenly distributed among the trapping beams with one inch e^{-1} beam waist.

4.3. Control and DAQ

Many atomic physics laboratories around the world have developed their own control system according to their experimental needs. One can find online examples ranging from completely open source [34] to semi-open source [35] and closed systems [36]. They all have two common fundamental characteristics: parallelism in the input/output signals and the ability to transport high speed 50 Ω signals. The former is achieved with a FPGA or a DSP core (or DAQ card) and the latter with a high-speed buffer.

In order to design our control system we thought of two generically different experimental sequences: (1) The most relevant parameter of the MOT to our current research interests is OD. We measure it as described in Sec. 4.2. This method requires two analog input/output channels with no major speed demand. (2) To generate photon pairs we need a duty cycle alternating MOT loading periods and FWM pulses, both in the order of hundreds of microseconds. As explained in Sec. 4.4 this can be achieved with 3 or 4 digital channels.

To achieve parallelism the core must have the complete sequence information before outputting any signal. For this to be possible it requires to access a physical memory device (RAM or ROM), storing the control sequence previously sent by the control host, a PC in our case, see Fig. 8. The time needed to deliver information from the host to the core, usually referred to as communication time, must be considered if multiple sequences are to be exported. It is typically in the order of hundreds of milliseconds; normally the core takes a few nanoseconds to access the device memory. This time should also be taken into account for the duty cycle repetition accuracy. Based on the number of digital and analog channels, and speed demands to carry out experiments, we selected the LabJack T7 [37] as the core of our control system.
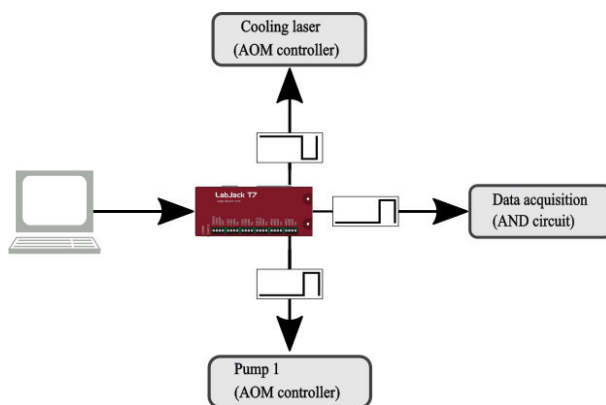

FIGURE 8. Block diagram of our control system. The experimental sequences are programmed in a PC. This information is sent to the chosen core, a LabJack T7 card, which in turn sends the coordinating signals to the experimental devices and the data acquisition system, see Sec. 4.3.2.

4.3.1. Using a LabJack T7

The LabJack T7 is an inexpensive DAQ card with 23 digital input/output channels, 2 analog outputs, and a 32 kB RAM memory card. It can be a good solution if its technical limits are well understood. Throughout developing this control system we tested its information management capacity and its time resolution.

The digital channels are driven by 23 registers of one bit each;[iv] each analog output is driven by a different 32-bit register. It is worth mentioning that an analog output is created by using a digital to analog converter (DAC). Therefore, a binary number represents a voltage. The possible values of the analog outputs and their resolution depend on the length of the register assigned to it. The later is calculated by dividing the full span of the output voltage (3.3 V) by the complete number of combinations given the number of registers, 2^{32} in this case.

The LabJack's RAM memory has 16-bit outputs (words) [38], therefore its core must create information packets of this size. In consequence all output registers (digital and analog) are connected to the RAM through a 16-bit buffer. Thus, all control sequences must be created using a 16-bit word convention. For example, if we had four 16-bit words in the RAM memory the first word could be used to drive the first 16 digital outputs (considering there are in total 23 digital outputs), the second word could drive the remaining 7 outputs (ignoring the remaining 9-bits), and the last two words would drive an analog output (given the fact that each analog output have a 32-bit resolution, it requires two 16 bit RAM words to be completely defined). Every access to a different RAM word has to be done in a different time slot, therefore only a 16-bit parallelism is achievable in the LabJack.

The time resolution of the Labjack's internal clock is $10\,\mu$s. This is the interval between accessing a memory and setting its information into an output register. In *stream mode* – the fastest to transfer information – the transmission frequency is 50 kHz [38]. Meaning that the complete sequence will be based on 20 μs time slots and its length will be limited by the RAM memory. Considering that 1 byte is equal to 8 bits and the 16-bit word convention, the maximum number of words is 16,384. The T7 allows either to work with 32-bits words in the case of analog outputs or to use the complete span over the digital outputs. In that case the maximum is reduced to 8,192 words. Thus, if we want to work with the minimum time scale and 16-bit RAM words, the LabJack would output all the data in 327.680 ms. This is more than enough for our current experimental needs. However, sequences requiring longer duty cycles – *e.g.* absorption imaging of cold atoms – may not be possible with the T7. If an analog output is used the resolution time is doubled because it needs 2 words per time slot to transmit the information; using the complete resources of the LabJack requires 4 words per time slot which is equal to 80 μs.

The T7 has a D-sub output that we used for wiring to the experimental setup by building a BNC terminal board [39].

Its output currents are low for driving 50 Ohm loads. Thus we built this board with a high speed buffer (Texas Instruments LMH6559) embedded on each channel. A two-rail power supply was used to bias the output buffers. The standby current consumption of all the buffered outputs is 500 mA. We wrote in Python a software to communicate a PC with the DAQ card. Its code and libraries are based on the vendors basic language, they are available in Ref. [39].

4.3.2. Data acquisition

Data acquisition for this experiment is also driven by a combination of commercial and home made instruments and software. It uses up to four avalanche photodiodes (APD, ID120-500-800) gated by AND circuits to a time-to-digital converter (id800TDC). The generated information is handled by an application written in Python. All APDs were calibrated through their bias voltages and operating temperatures. The quantum efficiency was set equal for all of them by adjusting individually the bias voltage whilst detecting a specific light intensity and wavelength. The operating temperatures were adjusted to $-40°$C to reduce the dark count rate (DCR) due to thermically-generated carriers in the detectors below 200 Hz. The data acquisition and control systems are synchronised through a home built AND circuit using a tri-state buffer (Texas Instruments SN74LVC126A) with a rising time of < 10 ns. This circuit serves for gating the output from our APDs to the id800TDC; our specific APD model is free-running and has no internal trigger mechanism. The APDs and the id800TDC operate with LVTTL signals while the LabJack T7 uses TTL pulses: this requires the AND circuit to down convert everything to LVTTL, acting as an interface between the two systems. More details about this AND circuit are found in Appendix A. One of the main constraints to design our data acquisition system was the software proprietary set by the manufacturer of the time tagger. This software would only run on 32-bit Windows, which was inefficient with our setup.[v] An in-house solution was developed in Python as a library for interfacing with the id800TDC. This library presents many advantages over the original software: flexibility of use, possibility of automation, and the modularity required for its integration with the rest of our software ecosystem. A graphical interface was also developed for calibration and real-time visualization purposes. Our software also allows processing of data outputted from the id800TDC to the computer in either batching or streaming modes depending on the memory load of the application and the extension of the experiment. This is possible because the id800TDC has data transfer rates up to 2.5 million events per second. For experiments in which a large number of photon events might cause memory issues the streaming mode allows the information to be directly written to a file. All the necessary code to setup a similar system is available in Ref. [40].

4.4. Pumping and detection

Four-wave mixing happens inside the science chamber that is located at the center of the schematics on Fig. 9, where the arrangements for the final preparation of the pump light and for the collection of the photon pairs are also depicted.

The three FWM beams, $p1$, $p2$ and the seed, are delivered to their distribution board, Fig. 9a). There, the three of them are collimated to a diameter of 1.1 mm with aspheric lenses (C230TMD-B) and are combined on the narrow-band interference filter IF1 (LL01-780-25) that transmits the 776 nm
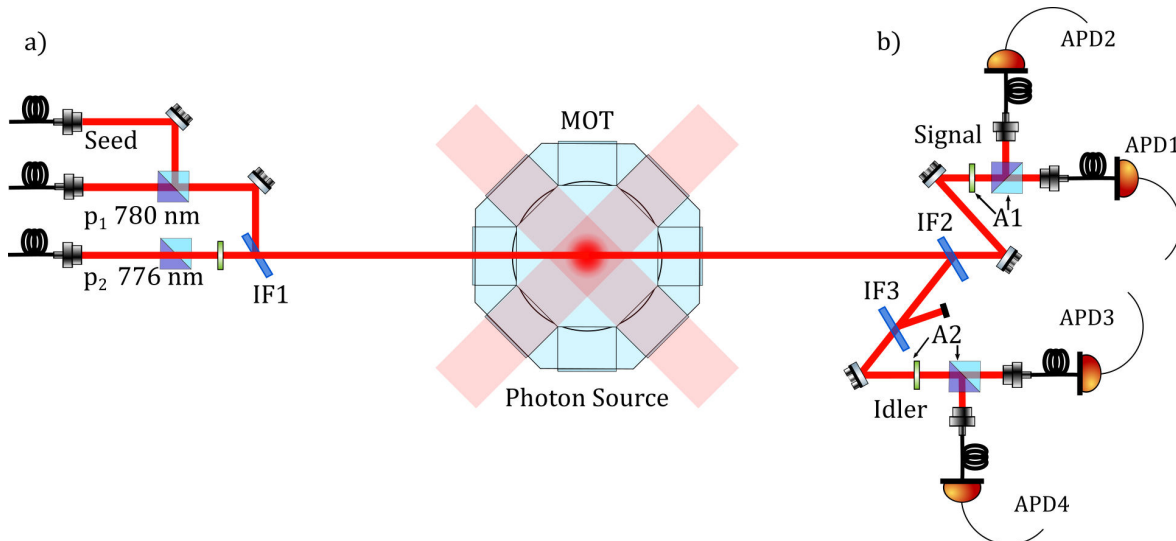

FIGURE 9. Schematics of the experimental setup to measure the time statistics of the photon pairs and their correlations in polarization: a) is the optics arrangement to collimate and combine the pump beams toward the center of the MOT and; b) is the optics for photon collection. The interference filter IF2 just transmits light with the signal frequency whereas IF3 transmits just idler photons and reflects all the pump beams remainders. Both output ports A1 and A2 couple each polarization component of the generated photons to an APD.

beam whilst reflecting light at the other two wavelengths. For the experiments reported here all polarizations were set linear. The three beams are overlapped in an optical path targeting the center of the atomic cloud. With this propagation geometry the mode-matching condition – Eq. (5) – is satisfied if the signal and the idler photons are generated in the same direction.

IF2 (LL01-780-25) allows just photons with the signal wavelength to pass through; IF3 (LL01-808-25) transmits the idler photon wavelength only. This array also filters the remainders of pump light in the photon flux that would appear as noise in our data. As depicted by Fig. 9b), both the signal and idler channels (A1 and A2) consist on a $\lambda/2$ and PBS arrangement enabling controllably splitting each photon flux in two inputs of fiber optics leading to the corresponding pair of avalanche detectors.

Light sources at 762 nm and 795 nm are required to align the signal and idler photons because both channels are filtered in frequency. The two outputs of the signal channel A1 are aligned by enhancing the FWM process with the seed beam [41]. This enables detecting 762 nm photons with a simple CMOS camera, which serves as the reference to couple these photons to the fibers of APD1 and APD2. Fibers leading the idler photons to APD3 and APD4 are aligned with the seed laser beam itself as the reference. Thus we typically reach a 70% fiber coupling efficiency using aspherical lenses (C230TMD-B). Our APDs have a nominal quantum efficiency close to 80 % around 780 nm.

The optical setup illustrated in Fig. 9b) has been designed for measuring the signal and iddler crossed correlations and the auto-correlations of each channel. Bi-photon correlations are measured by adjusting the $\lambda/2$ wave-plate for delivering all the light of each channel to a single APD. For auto-correlation experiments one can set each channel to split evenly its photon flux among the two detectors. Measurements of polarization correlations can be carried out as well since each APD is setup to measure just one projection of the generated photons.

A number of figures of merit have been designed to evaluate the generation of photon pairs. For this work we chose the coincidence rate since it is important for increasing the correlation histogram and the spectral brightness of the photon source (see Sec. 5). This parameter is optimized by a detuning $\Delta = -70$ MHz and a power of 500 μW for $p1$ and, a two-photon detuning $\delta = -3$ MHz and a 7 mW power for $p2$ in our setup; the FWM process is enhanced by setting the polarization of both pump beams linear and orthogonal to each other [42]. Figure 10 depicts the experimental duty cycle maximising the bi-photon coincidence rate. It consists on a loading time of 500 μs followed by a 200 μs pulse of FWM, when $p1$ and the AND circuits are switched on. Data acquisition is carried out during this period, without cooling light. The re-pump laser is left on at all times to maximize the number of atoms taking part in the double excitation scheme. The $p2$ beam is also switched on throughout the full duty cycle. This might be limiting our photon generation by expelling a
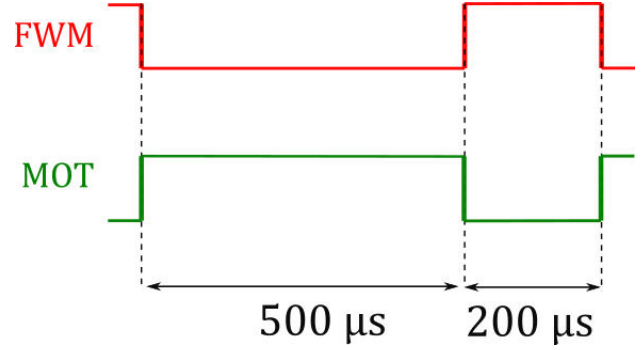

FIGURE 10. Experimental duty cycle optimizing the coincidence rate of photon pairs in our setup. It consists on a 500 μs MOT loading time (green) followed by a 200 μs FWM pulse (red). During the FWM stage the cooling light is switched off at the same time of switching on the pump beams and the AND gate. The re-pump and $p2$ beams are always switched on as well as the MOT coils.

few atoms from the MOT. We also leave the MOT coils switched on during the integration time. They generate a field around one Gauss at the atom-light interaction volume, close to the center of the MOT. This means that atoms are subject to a Zeeman shift in the order of 1.4 MHz during experiments. Our pump lasers have a bandwidth smaller than 250 kHz. We did not notice any effect of this magnetic field over the coherence results presented in Sec. 5. However, we might observe some of its influence over quantum polarization correlations during studies in the near future.

5. Measured coherence properties

With the setup described above we recorded the detection statistics of the photon pairs. Its behaviour is predicted by their second-order crossed-correlation function (which was derived in Sec. 3), and the auto-correlation function of each channel. With the former we were able to estimate the coherence time of the heralded idler photons and thus, the spectral brightness of our source. A brief theoretical discussion of the expected behavior of the auto-correlation functions $G_{ii}^{(2)}$ and $G_{ss}^{(2)}$ is given below. By measuring them it is confirmed that each decay channel corresponds to a chaotic source of photons, whose coherence time as such can be experimentally determined. Both results yield the required information to evaluate the classicality of the bi-photon temporal envelope through the Cauchy-Schwartz inequality.

5.1. Crossed- correlation function: coherence of the heralded photons

From Eq. (21) is reasonable to assume that the measured crossed-correlation function should fit

$$G_{si}^{(2)}(\Delta t) = G_{acc} + G_0 \exp(-\Delta t/\tau_c)\Theta(\Delta t), \qquad (26)$$

where G_0 is the maximum coincidence rate and

$$G_{acc} = R_1 R_2 \Delta t_{\text{bin}} T \qquad (27)$$

is the number of accidental coincidences. It is given by the coincidence rate expected from two uncorrelated random sources; R_1 and R_2 are the individual count rates measured at each APD; Δt_{bin} is the temporal bin width of the cross-correlation histogram and T the total integration time.

We fit the experimental data to the degree of second-order coherence, which is obtained by normalizing Eq. (26)

$$g_{si}^{(2)}(\Delta t) = \frac{G_{si}^{(2)}(\Delta t)}{G_{acc}}. \tag{28}$$

To make a more realistic model, one needs to introduce the noise probability distribution $f(\Delta t)$ of each APD. Assuming that Eq. (28) and $f(\Delta t)$ are two independent stochastic distributions, this measurement is expected to be a convolution of both of them. It is in general non-trivial to determine the function $f(\Delta t)$ of a detector. However, we found reasonable results by assuming that it is a Gaussian,

$$f(\Delta t) \propto \frac{1}{\tau_D \sqrt{2\pi}} \exp\left(-\frac{\Delta t^2}{2\tau_D^2}\right), \tag{29}$$

with a width τ_D that is related to the response time of the detectors. Carrying out the convolution results in the fitting function

$$g_{si(fit)}^{(2)}(\Delta t) = \frac{G_0}{2G_{acc}} \exp\left(\frac{\tau_D^2 - 2\Delta t \tau_c}{2\tau_c^2}\right) \tag{30}$$

$$\times \left[\text{erf}\left(\frac{\Delta t \tau_c / \tau_D - \tau_D}{\sqrt{2}\tau_c}\right) + 1\right]. \tag{31}$$

Coincidence histograms are obtained as explained in Sec. 4. Since FWM is pumped with two beams with orthogonal, linear polarization the signal beam is measured on transmission and the idler beam is measured on reflection from their corresponding PBS (Fig. 9). In this way, the accidental coincidences are attenuated by approximately one-third. For the experimental results here presented the parameters of the pump beams are those given in Sec. 4.4 except that, in this case, the two-photon detuning $\delta = +6$ MHz. The optical density is set to approximately 20, $T = 17$ s and $\Delta t_{\text{bins}} = 1.4$ ns.

Figure 11 shows the experimental data (black dots) for typical cross-correlation experiments in our setup. The dotted red curve is a fitting of Eq. (31) to these results leaving G_0, τ_D and τ_c as free parameters. One can immediately observe that the rise to its maximum value is smoother than the Heaviside function expected for ideal detection. The time dependency of these measurements is attenuated by the Gaussian noise distribution with bandwidth τ_D. The fitted curve is optimum for $\tau_D \sim 0.61$ ns, which is in the order of our detectors nominal response time (400 ps). From the exponential decay of the fitted curve we measured a heralded coherence time of $\tau_c = 4.41 \pm 0.09$ ns for the idler photons. In a purely atomic cascade decay this would be expected to be equal to the lifetime of the intermediate state $5P_{1/2}$ divided by 2π, *i.e.*
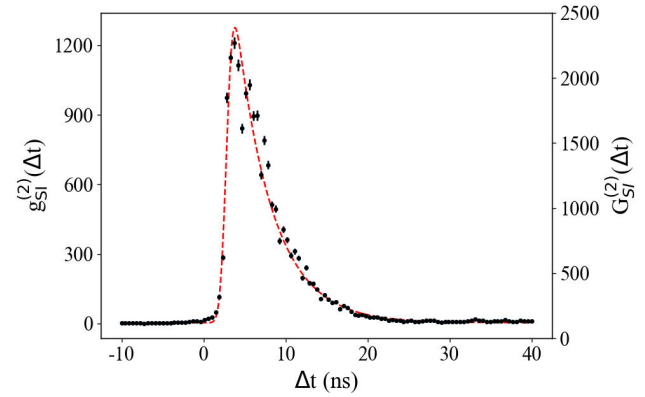

FIGURE 11. Cross-correlation histogram (black dots) as a function of the time delay between the signal and the idler photons. The right axis scales for the raw data whereas the left displays values for the normalized histogram. The red curve is a fit with Eq. (31). The best fitting parameters are $G_0 = 1654 \pm 48$, $\tau_D = 0.61 \pm 0.04$ ns and $\tau_c = 4.4 \pm 0.1$ ns.

4.40 ns. Note that a reduction with respect to this value would have been the result of collective effects in atomic ensembles [43].

We use two separate estimates of the accidental coincidences G_{acc}: either by their direct calculation, with Eq. (27), or by fitting the experimental data with Eq. (26). Calculation from the measured rates, $R_1 = 16,295$ s^{-1} and $R_2 = 15,860$ s^{-1}, and the time settings for these experiments yields $G_{acc} \sim 5.6$ s^{-1}. In order to obtain a reliable estimate from Eq. (27), we consider the longer coincidence time interval of $\Delta t = 350$ ns, resulting in $G_{acc} = 5.8 \pm 1.1$, compatible with the statistically inferred value.

The measured coherence time of the heralded idler photons corresponds to a bandwidth of 36.2 ± 0.8 MHz, which is a factor of ten smaller than the value obtained in experiments without cooling the atoms [41]. It in principle can be reduced to 20 MHz by optimizing the pumping parameters [15], and below 8 MHz by removing the time-dependent phases with a Fabry-Perot cavity and a electro-optic modulator [16]. The $5S_{1/2} \rightarrow 5P_{1/2}$ transition of ^{87}Rb has a natural linewidth of 5.75 MHz [33]. Thus heralded photons sourced in this way are suitable for interacting with atoms.

The spectral brightness of a quantum light source is likely to become a determining parameter to achieve control over the interaction of its photons with atoms. It is given by $B = 2\pi\tau_c r_c$, where $2\pi\tau_c$ is the inverse of its single-photon bandwidth, 2π (4.4 $\pm$ 0.1 ns) in our case. The coincidence rate r_c is obtained from the un-normalized histogram G_{SI}^2 plotted in Fig. 11. It is given by the number of coincidences detected during an integration window that we chose to be 40 ns. These yield a coincidence rate up to 10^4 s^{-1} under experimental conditions similar to the reported above but with $\delta = 0.5$ MHz. Thus we report here a spectral brightness around 280 coincidences s^{-1} MHz. This value is consistent with observations in similar sources [42] and two orders of magnitude larger than the value reported for hot atomic ensembles [41].

5.2. Auto-correlation functions: coherence properties of each channel.

Since the FWM process is induced on many atoms, each decay channel is a source of photons with chaotic origin. One can find their coherence properties through the treatment shown in Sec. 3.1, or by recalling that the first order correlation function of each atomic relaxation is given by the Fourier transform of its Lorentzian spectrum $S_i(\omega) = \Gamma_i/2[(\omega - \omega_i)^2 - (\Gamma_i/2)^2]$ [44];

$$G_{ii}^{(1)}(\Delta t) = \frac{1}{2\pi} \int_{-\infty}^{\infty} d\omega e^{i\omega \Delta t} S(\omega)$$

$$= G_0 e^{-i\omega_0 \Delta t} e^{-\Delta t/\tau_c}, \qquad (32)$$

where $G_0 \simeq \sqrt{G_{acc}}$ and τ_c is the coherence time of the chaotic photons, signal or idler. Due to their nature, in both cases, the second order of coherence is related to normalized first order correlation

$$g_{ii}^{(1)}(\Delta t) = \frac{G_{ii}^{(1)}(\Delta t)}{G_0}, \qquad (33)$$

by

$$g_{ii}^{(2)}(\Delta t) = 1 + |g_{ii}^{(1)}(\Delta t)|^2 = 1 + e^{-2|\Delta t|/\tau_c}, \qquad (34)$$

indicating an expected sharp time symmetry due to the absolute value in the exponent with an exponential decay with rate $\Gamma = 1/(2\pi\tau_c)$ towards negative and positive times.

To fit this data, the detectors noise was also assumed Gaussian. Its convolution with Eq. (34) is

$$g_{ii(fit)}^{(2)}(\tau) = \frac{1}{2} g_0 e^{\left(\frac{\tau_D^2 - 2\Delta t \tau_c}{2\tau_c^2}\right)} \left(\mathrm{erfc}\left[\frac{\tau_D^2 - \Delta t \tau_c}{\sqrt{2}\tau_D \tau_c}\right] \right.$$

$$\left. + e^{\frac{2\Delta t}{\tau_c}} \mathrm{erfc}\left[\frac{\tau_D^2 + \Delta t \tau_c}{\sqrt{2}\tau_D \tau_c}\right] \right). \qquad (35)$$

These experiments were performed by implementing a Hanbury Brown-Twiss interferometer at each output channel, A1 and A2, depicted on Fig. 9b). The photon flux of each one was evenly split at the PBS. Both reflecting and transmitting outputs were coupled into single-mode fibers and sent to their own APD.

The black dots in Fig. 12 display typical coincidence histograms for the signal (a) and idler (b) photons; the dashed, red curves are fitted to these data with Eq. (35). All the experimental parameters were set the same as for the cross-correlation plots except that the two photon detunings were $\delta = 4$ MHz and $\delta = 7$ MHz for (a) and (b) respectively and, the integration time was 20 minutes in both cases.

It is illustrative to point out the differences between these observations and the behaviour predicted for ideal detection. According to Eq. (34) the auto-correlation should present a maximum equal to 2 at the time zero. Neither the signal nor
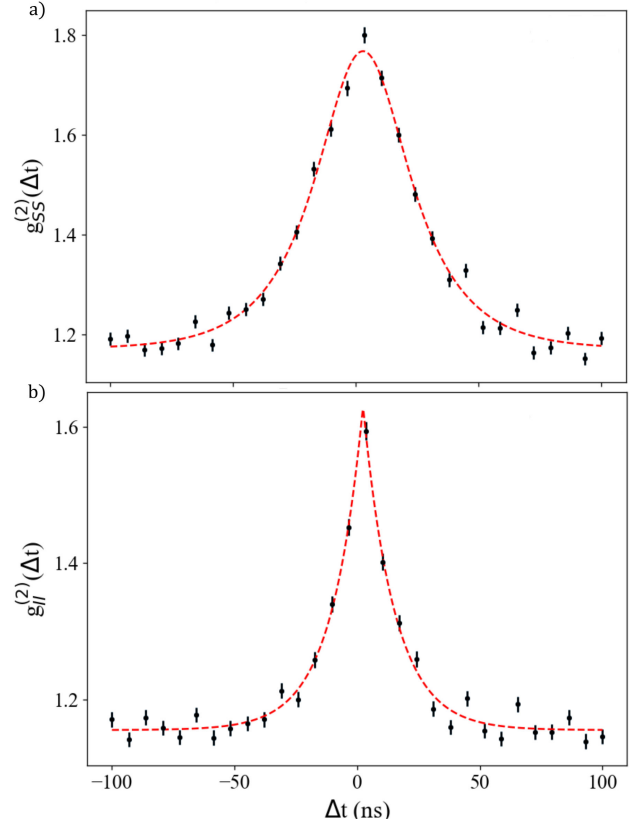

FIGURE 12. The black dots are the normalized autocorrelation histograms for a) signal and b) the idler photons. As expected, the auto-correlation $g_{ii}^{(2)}(\Delta t)$ approaches 1 for long integration times; an interval from -100 ns to 100 ns is enough to see this in our data. Both red curves represent the corresponding fits according to Eq. (35). In a) the best fitting parameters are $g_0 = 0.22 \pm 0.03$, $\tau_D = 9.77 \pm 2.12$ ns and $\tau_c = 18.92 \pm 2.65$ ns; in b) $g_0 = 0.12 \pm 0.03$, $\tau_D = 0.17 \pm 0.04$ ns and $\tau_c = 12.80 \pm 0.90$ ns.

TABLE I. Fit parameters τ_D and τ_c to the experimental data obtained for the cross-correlation, and the auto-correlation of the signal and idler photons; $g_{si}^{(2)}$, $g_{ss}^{(2)}$ and $g_{ii}^{(2)}$ respectively.

	$g_{SI}^{(2)}$	$g_{SS}^{(2)}$	$g_{II}^{(2)}$
τ_D (ns)	0.61 ± 0.04	9.77 ± 1.12	0.17 ± 0.04
τ_c (ns)	4.4 ± 0.1	18.9 ± 2.7	12.8 ± 0.9

the idler maximum reach this value because the APDs quantum efficiencies are lower than 100%. Furthermore, it was found that $g_{ss}^{(2)}(0) > g_{ii}^{(2)}(0)$, which is consistent with the greater quantum efficiency of our detectors at 762 nm than at 795 nm. Note that the experimental maxima have been smoothed by the noise bandwidth τ_D, which was left as a free parameter during the fittings. Their values, displayed on Table I, are different because the noise of the detectors is a function of the optical wavelength. In this case $\tau_{D762} > \tau_{D795}$ translates to a softer maximum for the signal auto-correlation.

The coherence time τ_c was left as a free parameter for these fits. Its values for the signal and idler photons are also displayed in Table I. They are consistently longer than the

coherence time of the heralded idler photons, as observed in similar sources of photon pairs [15].

5.3. Non-classicality

A vector analysis of the classical electromagnetic field, based on the Cauchy-Schwartz inequality, predicts that [45]

$$R = \frac{[g_{si}^{(2)}(\Delta t_{\max})]^2}{g_{ss}^{(2)}(0)g_{ii}^{(2)}(0)} \leq 1, \tag{36}$$

where $g_{si}^{(2)}(\Delta t_{\max})^2$, $g_{ss}^{(2)}(0)$ and $g_{ii}^{(2)}(0)$ are the maximum values of the second order of coherence measured from cross-correlations and autocorrelations. Their values, extracted from curves fitted to the experimental data shown in Figs. 11 and 12, are: $g_{si}^{(2)}(\Delta t_{\max}) = 1270 \pm 48$, $g_{ss}^{(2)}(\Delta t_{\max}) = 1.77 \pm 0.15$ and $g_{ii}^{(2)}(\Delta t_{\max}) = 1.63 \pm 0.14$. By plugging them into Eq. (36) one finds that $R = (5.62 \pm 1.38) \times 10^5$, which is evidence of a strong non-classical behavior in the time statistics of the photon pairs generated by our source.

6.   Conclusion and outlook

This article presented our source of photon pairs generated from cold atomic Rubidium samples. The employed experimental methods and techniques were described in detail. The idler photons have a heralded coherence time of 4.4 ± 0.1 ns. Together with the observed pair generation rates, which are in the order of 10^4 s^{-1}, this coherence time yields a spectral brightness three orders of magnitude larger than typical values achieved by sources based on hot atomic gases [41].

The reported results are a basic coherence characterisation of the generated photons pairs. Further insight is possible by replacing the presented model, which is purely atomic and is based on the Schrödinger equation, by a mathematical treatment of the Lindblad type. With the later is possible to systematically calculate atomic collective effects on the generated light, and to describe the bi-photon states in terms of their variables, as polarization and angular momentum. This would give a suitable guide for further experimental research seeking to achieve control over the generated quantum states with the valuable help of atomic spectroscopy.

Our source is bright and the generated light has a bandwidth suitable for interacting with atoms. Tailoring the bi-photon states would allow us to modulate this interaction with precision. The achievement of these goals would broaden the possibilities for building complete quantum systems of time-correlated photon pairs with atoms. One of several potential possibilities in such kind of system is to imprint and read memories using the bi-photons as the flying messengers of quantum information. This is the scientific pathway that we

have chosen for building an experimental scenario where exciting research on quantum information and its applications, like telecommunications and cryptography, can take place.

i. It has an approximate weight of 5 kg and a volume of about $50 \times 30 \times 20 \, \text{cm}^{-3}$; the vacuum quality has shown to be resilient to power cuts of the pump for longer than a few days, which makes the whole system suitable for transportation.

ii. It is desirable to form an evenly thin adhesive layer between post and granite. For this reason the Cretan Matterwaves Group chose Loctite 401 – the less viscous of these cyanoacrylate-based glues [25]. We opted for Loctite 495 instead since the number 401 was not domestically available.

iii. This laser was developed in collaboration with the Rydberg Quantum Optics Laboratory of Institute of Physics, UNAM. We made a few adaptations to replace some of the custom-machined parts with readily available off-the-bench components. It has been working almost non-stop for about three years with an excellent stability performance. Moreover we are building a low noise current supply with components that are readily acquirable in Mexico. We will make both the ECDL and the current supply designs available in a future publication.

iv. A register serves the sole purpose of storing the output value until the next one arrives. Therefore a time delay between the arrival of the information and its availability has to be taken into account.

v. According to the vendor the newer model provides native support for Python but we were unable to find information on the compatibility with other operating systems.

1. D. C. Burnham and D. L. Weinberg, *Observation of simultaneity in parametric production of optical photon pairs*, Phys. Rev. Lett. **25** (1970) 84. https://doi.org/10.1103/PhysRevLett.25.84.

2. S. J. Freedman and J. F. Clauser, *Experimental test of local hidden-variable theories*, Phys. Rev. Lett. **28** (1972) 938. https://doi.org/10.1103/PhysRevLett.28.938.

3. J. P. Dowling and G. J. Milburn, *Quantum technology: the second quantum revolution*, Phil. Trans. R. Soc. A. **361** (2003) 1655. https://doi.org/10.1098/rsta.2003.1227.

4. C. Couteau, *Spontaneous parametric down-conversion*, Contemp. Phys. **59** (2018) 291. https://doi.org/10.1080/00107514.2018.1488463.

5. A. Aspect, P. Grangier, and G. Roger, *Experimental realization of Einstein-Podolsky-Rosen-Bohm Gedankenexperiment: a new violation of Bell's inequalities*, Phys. Rev. Lett. **49** (1982) 91. https://doi.org/10.1103/PhysRevLett.49.91.

6. L. M. Duan, M. Lukin, J. I. Cirac, and P. Zoller, *Long-distance quantum communication with atomic ensembles and linear optics*, Nature **414** (2001) 413. https://doi.org/10.1038/35106500.

7. Y.W. Cho, G. Campbell, J. Everett, J. Bernu, D. Higginbottom, M. Cao, J. Geng, N. Robins, P. Lam, and B. Buchler, *Highly efficient optical quantum memory with long coherence time in cold atoms*, Optica **3** (2016) 100. https://doi.org/10.1364/OPTICA.3.000100.

8. J. Guo, X. Feng, P. Yang, Z. Yu, L. Chen, C.H. Yuan, and W. Zhang, *High-performance Raman quantum memory with optimal control in room temperature atoms*, Nat. Commun. **10** (2019) 1. https://doi.org/10.1038/s41467-018-08118-5.

9. M. Wallquist, K. Hammerer, P. Rabl, M. Lukin, and P. Zoller, *Hybrid quantum devices and quantum engineering*, Phys. Scr. **T137** (2009) 014001. https://doi.org/10.1088/0031-8949/2009/T137/014001.

10. G. Kurizki, P. Bertet, Y. Kubo, K. Mølmer, D. Petrosyan, P. Rabl, and J. Schmiedmayer, *Quantum technologies with hybrid systems*, Proc. Natl. Acad. Sci. U. S. A. **112** (2015) 3866. https://doi.org/10.1073/pnas.1419326112

11. A. Kuzmich, W. Bowen, A. Boozer, A. Boca, C. Chou, L.M. Duan, and H. Kimble, *Generation of nonclassical photon pairs for scalable quantum communication with atomic ensembles*, Nature **423** (2003) 731. https://doi.org/10.1038/nature01714

12. J. K. Thompson, J. Simon, H. Loh, and V. Vuletić, *A high-brightness source of narrowband, identical-photon pairs*, Science **313** (2006) 74. https://doi.org/10.1126/science.1127676

13. T. Chaneliere, D. Matsukevich, S. Jenkins, T. Kennedy, M. Chapman, and A. Kuzmich, *Quantum telecommunication based on atomic cascade transitions*, Phys. Rev. Lett. **96** (2006) 093604. https://doi.org/10.1103/PhysRevLett.96.093604

14. S. Du, P. Kolchin, C. Belthangady, G. Y. Yin, and S. E. Harris, *Subnatural linewidth biphotons with controllable temporal length*, Phys. Rev. Lett. **100** (2008) 183603. https://doi.org/10.1103/PhysRevLett.100.183603

15. B. Srivathsan, G. K. Gulati, B. Chng, G. Maslennikov, D. Matsukevich, and C. Kurtsiefer, *Narrow band source of transform-limited photon pairs via four-wave mixing in a cold atomic ensemble*, Phys. Rev. Lett. **111** (2013) 123602. https://doi.org/10.1103/PhysRevLett.111.123602

16. M. A. Seidler, X. J. Yeo, A. Ceré, and C. Kurtsiefer, *Spectral compression of narrowband single photons with a resonant cavity*, Phys. Rev. Lett. **125** (2020) 183603. https://doi.org/10.1103/PhysRevLett.125.183603.

17. R. T. Willis, F. E. Becerra, L. A. Orozco, and S. L. Rolston, *Photon statistics and polarization correlations at telecommunications wavelengths from a warm atomic ensemble*, Opt. Express **19** (2011) 14632. https://doi.org/10.1364/OE.19.014632.

18. G. K. Gulati, B. Srivathsan, B. Chng, A. Ceré, and C. Kurtsiefer, *Polarization entanglement and quantum beats of photon pairs from four-wave mixing in a cold 87Rb ensemble*, New J. Phys. **17** (2015) 093034. http://dx.doi.org/10.1088/1367-2630/17/9/093034.

19. T.M. Zhao, Y. S. Ihn, and Y.H. Kim, *Direct generation of narrow-band hyperentangled photons*, Phys. Rev. Lett. **122** (2019) 123607. https://doi.org/10.1103/PhysRevLett.122.123607.

20. J. Wen and M. H. Rubin, *Transverse effects in paired-photon generation via an electromagnetically induced transparency medium. I. Perturbation theory*, Phys. Rev. A **74** (2006) 023808. https://doi.org/10.1103/PhysRevA.74.023808.

21. M. O. Scully and M. S. Zubairy, Quantum optics, 1st ed. (Cambridge University Press, 1999), pp. 616-618. https://doi.org/10.1119/1.19344.

22. F. E. Becerra, R. T. Willis, S. L. Rolston, H. J. Carmichael, and L. A. Orozco, *Nondegenerate four-wave mixing in rubidium vapor: Transient regime*, Phys. Rev. A **82** (2010) 043833. `https://doi.org/10.1103/PhysRevA.82.043833`.

23. C. A. Kocher, *Time correlations in the detection of successively emitted photons*, Ann. Phys. **65** (1971) 1. `https://doi.org/10.1016/0003-4916(71)90159-X`

24. C. Stroud Jr, J. Eberly, W. Lama, and L. Mandel, *Superradiant effects in systems of two-level atoms*, Phys. Rev. A **5** (1972) 1094. `https://doi.org/10.1103/PhysRevA.5.1094`

25. D. Sahagun, V. Bolpasi, and W. von Klitzing, *A simple and highly reliable laser system with microwave generated repumping light for cold atom experiments*, Opt. Commun. **290** (2013) 110. `https://doi.org/10.1016/j.optcom.2012.10.013`

26. P. K. Mandal, V. Naik, V. Dev, A. Chakrabarti, and A. Ray, *Blue fluorescence as a frequency offset reference in the rubidium 5S-5P-5D transition*, Appl. Opt. **57** (2018) 3612. `https://doi.org/10.1364/AO.57.003612`

27. T. T. Grove, V. Sanchez-Villicana, B. Duncan, S. Maleki, and P. Gould, *Two-photon two-color diode laser spectroscopy of the Rb 5D5/2 state*, Phys. Scr. **52** (1995) 271. `https://doi.org/10.1088/0031-8949/52/3/008`

28. M. L. Harris, C. S. Adams, S. L. Cornish, I. C. McLeod, E. Tarleton, and I. G. Hughes, *Polarization spectroscopy in rubidium and cesium*, Phys. Rev. A **73** (2006) 062509. `https://doi.org/10.1103/PhysRevA.73.062509`

29. D. J. Thompson and R. E. Scholten, *Narrow linewidth tunable external cavity diode laser using wide bandwidth filter*, Rev. Sci. Instrum. **83** (2012) 023107. `https://doi.org/10.1063/1.3687441`

30. R. Barger and J. Hall, *Pressure shift and broadening of methane line at 3.39 μ studied by laser-saturated molecular absorption*, Phys. Rev. Lett. **22** (1969) 4. `https://doi.org/10.1103/PhysRevLett.22.4`

31. H. H. Jen, *Spectral analysis for cascade-emission-based quantum communication in atomic ensembles*, J. Phys. B: At. Mol. Opt. Phys. **45** (2012) 165504. `https://doi.org/10.1088/0953-4075/45/16/165504`

32. H. J. Metcalf and P. V. der Straten, Laser Cooling and Trapping (Springer NY, 1999), pp. 25-26. `https://doi.org/10.1007/978-1-4612-1470-0`

33. D. A. Steck, `http://steck.us/alkalidata`.

34. Atom Optics Laboratory, University of Texas at Austin, `http://m-labs.hk/experiment-control/sinara-core/`A Laboratory Control System for Cold Atom Experiments (2015).

35. European Laboratory for Non-Linear Spectroscopy, `https://ew.lens.unifi.it/`. DIO128-Board Based Aquisition System (2005).

36. M. Senn, `http://m-labs.hk/experiment-control/sinara-core/` Sinara hardware. 2020. M-Labs

37. LabJack Corporation, `https://labjack.com/products/t7`.

38. LabJack Corporation, `https://labjack.com/support/datasheets/t-series/communication/stream-mode/stream-out`

39. R. A. Gutierrez-Arenas, (2021). `https://doi.org/10.5281/zenodo.5062126`

40. L. Y. Villegas-Aguilar, `https://doi.org/10.5281/zenodo.4299245` (2020).

41. R. Willis, F. Becerra, L. Orozco, and S. Rolston, *Four-wave mixing in the diamond configuration in an atomic vapor*, Phys. Rev. A **79** (2009) 033814. `https://doi.org/10.1103/PhysRevA.79.033814`

42. A. Ceré, B. Srivathsan, G. K. Gulati, B. Chng, and C. Kurtsiefer, *Characterization of a photon-pair source based on a cold atomic ensemble using a cascade-level scheme*, Phys. Rev. A **98** (2018) 023835. `https://doi.org/10.1103/PhysRevA.98.023835`

43. N. E. Rehler and J. H. Eberly, *Superradiance*, Phys. Rev. A **3** (1971) 1735. `https://doi.org/10.1103/PhysRevA.3.1735`

44. H. Carmichael, Statistical Methods in Quantum Optics, 2nd ed. (Springer Science & Business Media, NY, 2002), pp. 45-47. `https://doi.org/10.1007/978-3-662-03875-8`

45. M. Reid and D. Walls, *Violations of classical inequalities in quantum optics*, Phys. Rev. A **34** (1986) 1260. `https://doi.org/10.1103/PhysRevA.34.1260`

46. R. A. de Oliveira *et al.*, *Nonlinear optical memory for manipulation of orbital angular momentum of light*, Opt. Lett. **40** (2015) 4939. `https://doi.org/10.1364/OL.40.004939`